

Large negative magnetoresistance in BaMn_2Bi_2 antiferromagnet

Takuma Ogasawara,¹ Kim-Khuong Huynh,^{2,*} Time Tahara,³ Takanori Kida,³ Masayuki Hagiwara,³ Denis Arçon,^{4,5} Motoi Kimata,⁶ Stephane Yu Matsushita,² Kazumasa Nagata,¹ and Katsumi Tanigaki^{2,7,†}

¹*Department of Physics, Graduate School of Science,
Tohoku University, 6-3 Aramaki, Aoba, Miyagi, Japan*

²*AIMR, Tohoku University, 1-1-2 Katahira, Aoba, Sendai, Miyagi, Japan*

³*Center of Advanced High Magnetic Field Science,
Graduate School Science, Osaka University,
Machikaneyama, Toyonaka, Osaka, Japan*

⁴*Faculty of mathematics and physics, University of Ljubljana,
Jadranska c. 19, 1000 Ljubljana, Slovenia*

⁵*Jozef Stefan Institute, Jamova c. 39, 1000 Ljubljana, Slovenia*

⁶*Institute for Materials Research, Tohoku University
2-1-1 Katahira, Aoba-ku, Sendai 980-8577, Japan*

⁷*BAQIS, Bld. 3, No.10 Xibeiwang East Rd.,
Haidian District, Beijing 100193, China*

(Dated: February 18, 2021)

Abstract

A very large negative magnetoresistance (LNMR) is observed in the insulating regime of the antiferromagnet BaMn_2Bi_2 when a magnetic field is applied perpendicular to the direction of the sublattice magnetization. High perpendicular magnetic field eventually suppresses the insulating behavior and allows BaMn_2Bi_2 to re-enter a metallic state. This effect is seemingly unrelated to any field induced magnetic phase transition, as measurements of magnetic susceptibility and specific heat did not find any anomaly as a function of magnetic fields at temperatures above 2 K. The LNMR appears in both current-in-plane and current-out-of-plane settings, and Hall effects suggest that its origin lies in an extreme sensitivity of conduction processes of holelike carriers to the infinitesimal field-induced canting of the sublattice magnetization. The LNMR-induced metallic state may thus be associated with the breaking of the antiferromagnetic parity-time symmetry by perpendicular magnetic fields and/or the intricate multi-orbital electronic structure of BaMn_2Bi_2 .

I. INTRODUCTION

Numerous exotic materials adopt the tetragonal ThCr_2Si_2 (122) crystallographic structure [Fig. 1(a)], and more than 400 compounds have been known¹ to be classified into this structure. An extended family related to BaFe_2As_2 also belongs to this large family. Since the high temperature superconductivity was found for the BaFe_2As_2 family of compounds by chemically doping or under high pressure^{2,3}, researchers have systematically studied on almost all possible combinations in the formula of BaTM_2Pn_2 , where TM stands for 3d-transition metals and Pn pnictogen elements. The flexibility of the tetragonal (122) structure allows the TM site to be replaced by many 3d elements from Cr to Zn, resulting in a wide variety of materials hosting diverse ground states. For instance, BaCr_2As_2 is a G-type (checkerboard) antiferromagnetic (G-AFM) metal with large holelike Fermi surfaces^{4,5}; BaCo_2As_2 is a paramagnetic metal close to a magnetic quantum critical point⁶⁻⁹; BaCu_2As_2 is a weakly correlated *sp* metal^{10,11}; BaNi_2As_2 is a superconductor with a conventional electron-phonon coupling mechanism^{12,13}; and BaZn_2As_2 is potentially a host material for diluted magnetic semiconductors¹⁴⁻¹⁷.

A subfamily of BaMn_2Pn_2 (*Pn*: P, As, Sb, and Bi) compounds can be differentiated from the other BaTM_2Pn_2 's for their remarkable ground states with a parity-time symmetry¹⁸, orbital-selective magnetism¹⁹, and intriguing transport properties²⁰. Unlike most of the other TM's, where stable BaTM_2Pn_2 phases are only available with P and As, Mn forms a complete set of BaMn_2Pn_2 compounds with all pnictogen elements from P to Bi. Except for the highly insulating BaMn_2P_2 , the other BaMn_2Pn_2 's, BaMn_2As_2 , BaMn_2Sb_2 , and BaMn_2Bi_2 , exhibit the behaviors of semiconducting-like antiferromagnets with a common G-type antiferromagnetic (AFM) order with high Néel temperatures (T_N 's)²⁰. As we reported recently, these compounds interestingly exhibit an unusual and very large magnetoresistance (LNMR)²⁰ under a modest magnetic field of 16 T. The properties of the LNMR found in the BaMn_2Pn_2 's antiferromagnets do not fit to any known models for magnetoresistance, and its mechanism remains to be an open question. Recent theoretical and experimental studies have pointed out a rather intricate magnetic-electronic nature of these materials¹⁸⁻²⁰. The symmetry of the AFM order of BaMn_2Pn_2 (point group $4'/m'mm'$) breaks both time reversal (TR) and space inversion (SI) symmetries, but the combined parity-time (PT) symmetry is preserved¹⁸. The *d-p* states resulting from this magnetic-electronic entangled

states reside at the top of the valence band¹⁸. Therefore the transport properties of the holelike carriers can be highly susceptible to the perturbations of the magnetic order caused by an external magnetic field \mathbf{H} . The origin of the LNMR observed for BaMn_2Pn_2 's may thus be associated with the breaking of the PT symmetry in the applied \mathbf{H} ²⁰. On the other hand, another theoretical study based on dynamical density functional calculations suggests an intricate orbital-selective magnetism¹⁹. Whereas the out-of-plane d orbitals of Mn form strongly Mott localized band residing far from the Fermi level (E_F) in an agreement with the G-type AFM order, the bands originated from the in-plane orbitals are nonmagnetic. The xy band is even more interesting because it is not fully insulating even under high Coulomb interaction U , resulting in a small density of holelike states at E_F . These states are of the most importance from the viewpoint of transport properties and can be directly related to the LNMR.

Among pnictogen elements, bismuth has the strongest spin-orbit coupling (SOC) and the largest radii of atomic wavefunctions; the latter gives the strongest d - p hybridization. In our previous research, BaMn_2Bi_2 exhibits the largest LNMR in the smallest range of magnetic field strength (H) in relative to other BaMn_2Pn_2 's. Therefore, BaMn_2Bi_2 could be the key compound for understanding the observed LNMR. In the present paper, we report the detailed measurements of the electrical transport, thermodynamic, and magnetic properties of BaMn_2Bi_2 . The isobaric specific heat C_p and magnetic susceptibility χ shows no detectable structural and/or magnetic transition below T_N even under high H . Our measurements of the magnetotransport properties include both the in-plane (electric current \mathbf{j} parallel to the ab conduction layer) and the out-of-plane (\mathbf{j} along to the c -axis) for various directions of \mathbf{H} and at different temperatures. We found that the LNMR manifests in both current-in-plane and current-out-of-plane configurations. Regardless of the direction of the electric current \mathbf{j} in relative to the crystal axes, the conductivity of BaMn_2Bi_2 in both current-in-plane and current-out-of-plane settings is maximized when \mathbf{H} lies in the ab plane, i.e. perpendicular to the direction of the sublattice magnetization of the G-type AFM order. The electrical transport of BaMn_2Bi_2 is thus sensitive even to the small \mathbf{H} -induced in-plane magnetization, the later of which breaks the PT-symmetry.

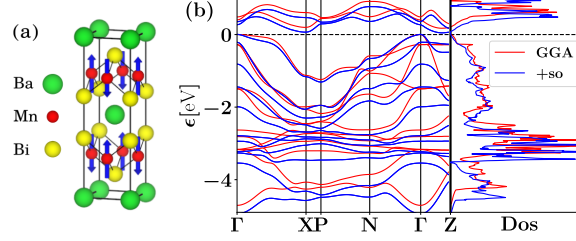


Fig. 1. (a) crystal structure and G-type antiferromagnetic order of BaMn_2Bi_2 . (b) band structure and density of states of BaMn_2Bi_2 with and without spin-orbit coupling.

II. RESULTS

A. Electronic structure

In order to understand the electronic structure of BaMn_2Bi_2 , we performed Density Functional Theory (DFT) calculations employing the WIEN2k code, which implements a full-potential linearized augmented plane-wave LAPW + local orbitals method²¹. We used the experimental information of the crystal lattice and the magnetic ordering²² as the input parameters (see Sec. V). To confirm the effect of SOC on the electronic structure, we compare the results of DFT (using GGA approximation) with and without SOC [Fig.1(b)]. Turning on the SOC does not change the electronic structure qualitatively, however the bandgap decreases and a degeneracy of the second hole band is lifted. Similar calculations for BaMn_2As_2 yielded an electronic structure with the effect of SOC being much smaller in line with a smaller SOC of As element, which is in agreement with the experimental results of ARPES measurements²³. We thus conclude that SOC has the largest effect on the electronic structure for BaMn_2Bi_2 within the BaMn_2Pn_2 family of compounds.

B. Large negative magnetoresistance (LNMR)

1. Current-in-plane magnetoresistance

Fig. 2(a) and (b) show the T -dependencies of ρ_a of a BaMn_2Bi_2 single crystal measured different strengths of \mathbf{H} parallel to the a -axis of the crystal. These measurements were done in the in-plane configuration, and both \mathbf{j} and \mathbf{H} were directed along the crystallographic

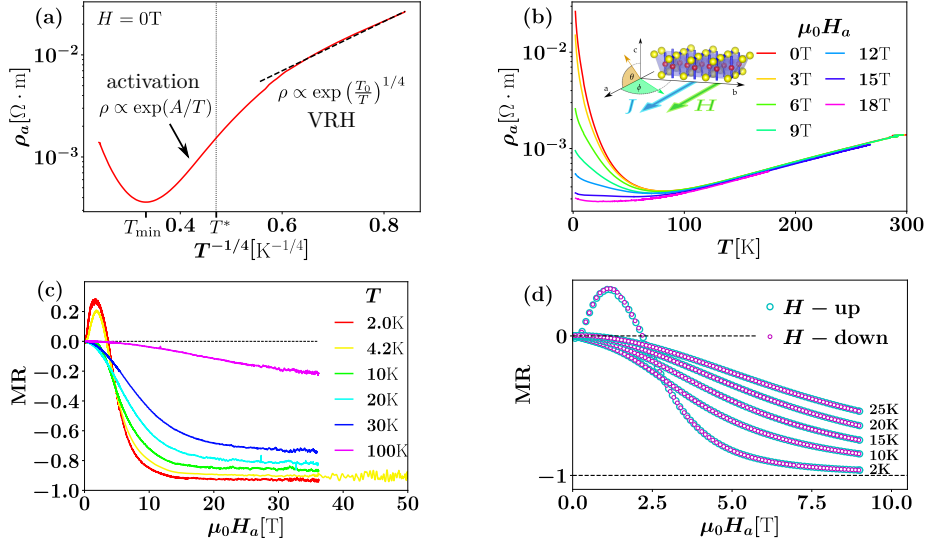


Fig. 2. (Color online) (a) Temperature dependence of ρ_a at 0 T plotted as a function of $T^{-1/4}$. The dashed line show the fitting using a variable range hopping rule for the data at low temperatures. (b) Temperature dependencies of the in-plane electrical resistivity (ρ_a) of BaMn_2Bi_2 measured under different strengths of perpendicular magnetic fields (H_a). The electric current \mathbf{j} was applied along the a -axis [inset]. (c) Longitudinal MR ($\theta = 0^\circ$) observed at various T 's. (d) No hysteresis was observed in scanning H_{ab} both in increasing and decreasing modes.

a -axis, i.e., perpendicular to the easy c -axis of the G-type AFM order. The dependence of resistivity on temperature of BaMn_2Bi_2 is similar to those found for all BaMn_2Pn_2 's, however BaMn_2Bi_2 is much more conductive²⁰. As shown in Fig. 2(a), the zero-field $\rho_a(T)$ curve first decreases with decreasing temperatures, but then reaches a broad minimum before it starts to increase on further cooling. This metal-to-insulator cross-over (MIC) occurs at $T_{\min} \approx 83$ K, being apart from the Néel temperature $T_N = 387$ K²⁴. Below the MIC, the $\rho_a(T)$ curve can be fitted by an activation law $\rho_a(T) \propto \exp(A/T)$ down to $T^* \approx 20$ K (the fit is not shown). At lower temperatures, the $\rho_a(T)$ curve exhibits the rule of Mott's three-dimensional variable range hopping (VRH) described as $\rho \propto \exp[(T/T_0)^{1/4}]$. That suggests the insulating behaviors at $T < T_{\min}$ is not caused by a bandgap but rather due to a localization of charge carriers. Interestingly, when $\mathbf{H} \parallel a$ is turned on, a very large negative MR appears at $T < 83$ K and reduces ρ_a significantly. As a result, the low-temperature insulating trend of ρ_a is suppressed by strong H_a , and BaMn_2Bi_2 exhibits a bad metallic

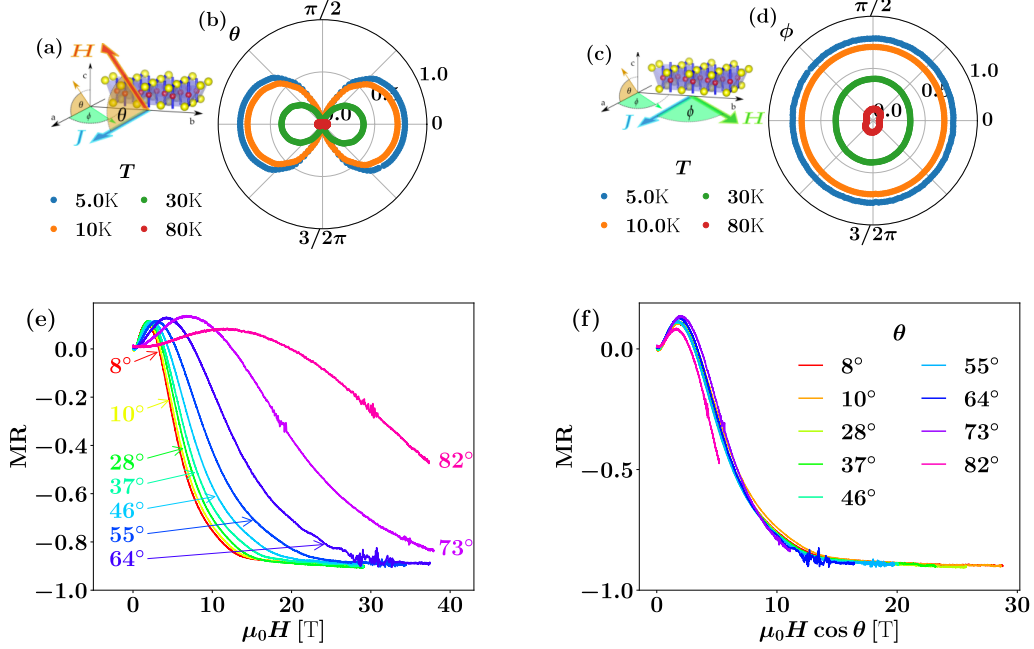


Fig. 3. (a) The setting for the measurements of angle resolved MR with current-in-plane in θ rotation of H . (b) The absolute values of MR as function of θ in polar plot. (c) and (d) are same of (a) and (b) in ϕ rotation of H . (e) The magnetic field dependence of MR for various θ s. (f) MR scaled by in-plane magnetic field $\mu_0 H \cos \theta$

behavior at $\mu_0 H_a = 18$ T.

As shown in Fig.2(c), the LNMR is strongly dependent on temperatures. At the lowest T achieved in the present measurements, LNMR exhibits a pronounced bell-shaped field dependence. For instance, at $T = 2$ K, with turning on H_a the longitudinal MR at first increases to a maximum MR $\approx +40\%$ at $H_a \approx 1.7$ T. As H_a increases, MR drops quickly to the negative values ending up by bending to a saturation of MR $\approx -96\%$ at $\mu_0 H_a \approx 16$ T. This corresponds to the metallic state being re-entered in the $\rho_a(T)$ curve. With further increase of H_a , an almost constant MR can be realized up to the highest H_a of 55 T. As T increases, the positive component in MR fades away and disappears at $T^* \approx 20$ K, leaving only the negative MR at elevated T 's. The values of the saturated negative MR also reduce with increasing T and stronger H_a 's are needed for returning the MR back to the same saturation realized at lower T . In Fig.2(d), the MR curves under increasing and decreasing H_a 's totally overlap on each other, and no hysteresis was observed. This suggests that the origin of the LNMR is apart from a \mathbf{H} -induced first order phase transition²⁵.

The LNMR in BaMn₂Bi₂ shows an interesting angular dependence on the direction of \mathbf{H} . Figs. 3(a) and (b) show that the LNMR is very sensitive to the angle θ that \mathbf{H} makes with the ab -plane. A \mathbf{H} aligned within the ab plane maximizes the LNMR, and with \mathbf{H} rotating away from basal plane, the magnitude of the LNMR quickly reduces. Individual H_a scans at different θ angles displayed in Fig. 3(e) show that the MR curves are elongated toward higher H_a values as θ increases. This strong out-of-plane anisotropy results in a curious horizontal eight-figure shape as the absolute value of the LNMR is plotted against θ in the polar coordinate representation shown in Fig. 3(a). On the contrary, the LNMR effectively remains in its maximized value as \mathbf{H} rotates within the ab -plane [Figs. 3(e)]. Changing the ϕ -angle from 0° to 90° , i.e., from being parallel to anti-parallel with the current \mathbf{j} and the a axis, yields only an insignificant angular dependence. The angle resolved measurements suggest that the component of the magnetic field lying in the crystallographic ab -plane and perpendicular to the AFM sublattice magnetization, \mathbf{H}_{ab} , plays a crucial role in the mechanism of the LNMR. In Fig. 3(f), when the MR curves collected at different θ angles are plotted versus the in-plane component of magnetic fields, i.e. $H_a = H \cos \theta$, almost all the MR curves scales to a single H_a -dependence. However, there are some discrepancies coming from the MR curves measured at large θ 's, at which the out-of-plane component H_c of the magnetic field is larger than the in-plane H_a . These may indicate that the positive component of the MR has an additional dependence on H_c . This is different from the H -dependence of the negative MR component, which shows a very good scaling with respect to $H \cos \theta$.

2. Current-out-of-plane magnetoresistance

The angular dependence of the LNMR described in the previous section suggests that the magnetoconductivity of BaMn₂Bi₂ is mainly determined by the strength of the in-plane magnetic field \mathbf{H}_{ab} , being regardless of the angle between \mathbf{H}_{ab} and the electric current \mathbf{j} . In order to confirm this, we carried out current-out-of-plane measurements with \mathbf{j} flowing along the c -axis, i.e. being parallel to the easy axis of the AFM. Figs. 4(a) and (b) show that the LNMR also appears under the \mathbf{H}_a with a dependence on the field strength H_a and temperatures being very similar to that seen in the in-plane LNMR ($\mathbf{j} \parallel ab$). Fig. 5 shows additional experiments for angular-dependence of the out-of-plane LNMR under rotating \mathbf{H} .

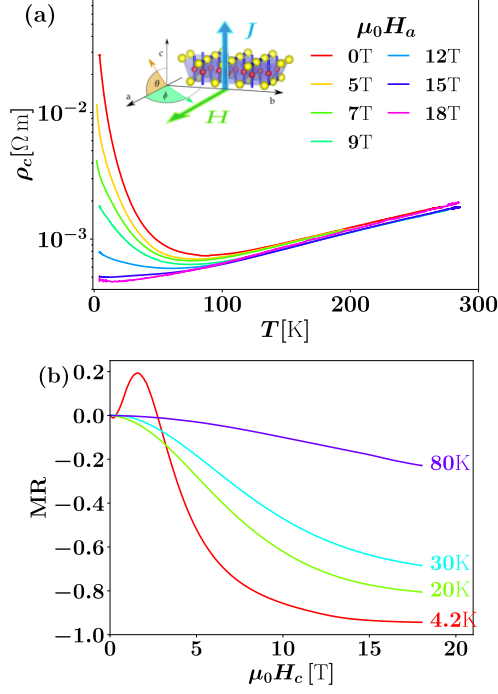


Fig. 4. (Color online) (a) Temperature (T) and magnetic field (H) dependence of electrical resistivity (ρ_c) of BaMn_2Bi_2 when the electric current \mathbf{j} is parallel to the \hat{c} -axis (out-of-plane geometry). (b) MR observed at various T 's. Negative MR becomes larger with a decrement in T . The positive MR is only observed at T 's lower than T^* under weak $\mu_0 H$.

The results follow the same trend with those observed in current-in-plane settings, i.e. the LNMR is very anisotropic with respect to the θ angle and show only a small modulation versus ϕ .

As described so far, the LNMR as a function of T and \mathbf{H} is very similar between current-in-plane and current-out-of-plane settings. It is solely determined by the direction of \mathbf{H} , and achieves the largest value when \mathbf{H} is perpendicular to the sublattice magnetization of the AFM ground states with the PT symmetry. These experimental results may imply that the LNMR is likely associated with the breaking of symmetry in the AFM ordered ground state of this system.

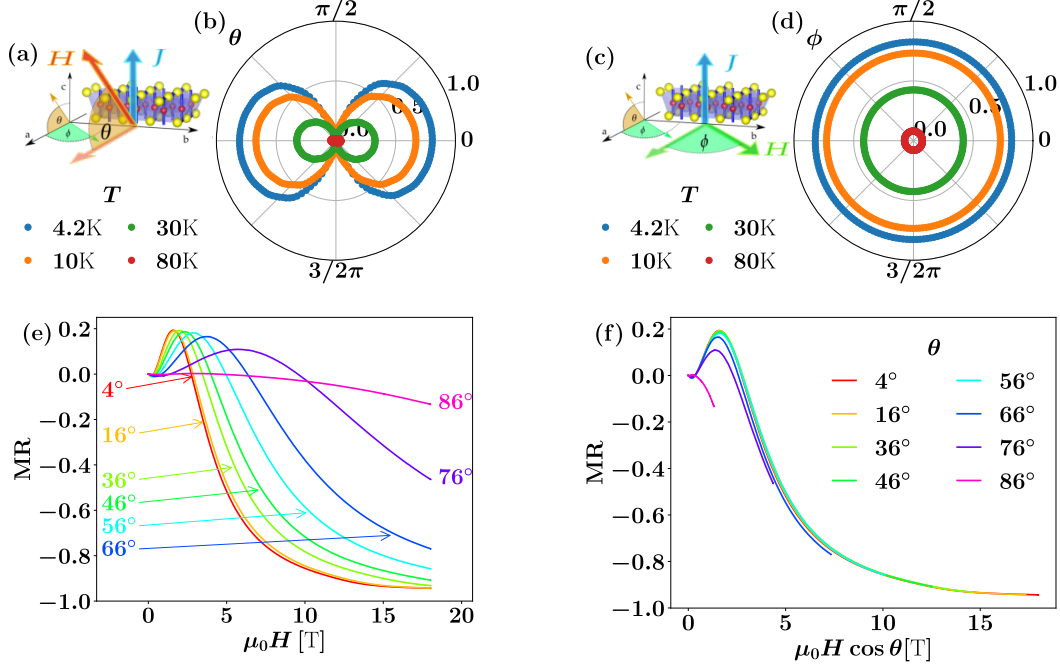


Fig. 5. (a) The setting for the measurements of angle resolved MR with current-out-of-plane in θ rotation of H . (b) The absolute values of MR as function of θ in polar plot. (c) and (d) are same of (a) and (b) in ϕ rotation of H . (e) The magnetic field dependencies of MR for various θ s. (f) MR scaled by in-plane magnetic field $\mu_0 H \cos \theta$.

C. Transverse Hall effects

The transverse Hall resistivity for both in-plane and out-of-plane configurations was measured to investigate the temperature dependence of carrier characteristics. In the in-plane (out-of-plane) configuration, ρ_{yx} (ρ_{xz}) was measured as \mathbf{H} was parallel to the c -axis (a -axis) and \mathbf{j} was along the a -axis (c -axis) at different T 's. The in-plane configuration yields an ρ_{yx} that increases linearly with H_c for $T \geq 20$ K, indicating that a single holelike carrier type is dominant [Fig. 6(a)]. The linear H_c -dependence, however, gradually turns into a non-linear one as T decreases further. The slopes of $\rho_{yx}(H_c)$ curves around $H_c \approx 0$ decrease to zero and eventually cross to the negative side at $T^* \approx 20$ K, while they remain bending towards the positive side under high H_c . The onset of the non-linear $\rho_{yx}(H_c)$ occurs at T^* , where the positive component in MR simultaneously starts to appear.

In order to estimate the mobility and number of the carriers at $T > T^*$, we fitted the $\rho_{yx}(H_c)$ curves using a linear one-carrier-type model, respectively. In Fig. 7(b) the fitting

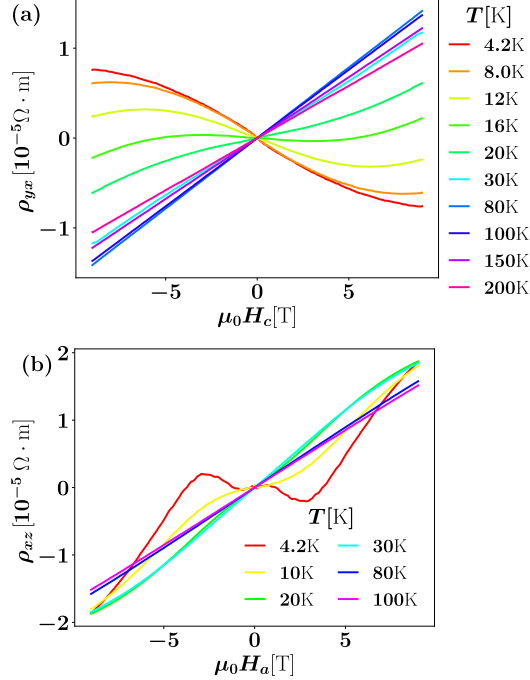


Fig. 6. (Color online) H_c -dependences of (a) ρ_{yx} (current-in-plane) and (b) ρ_{xz} (current-out-of-plane) measured at various T 's under $\mathbf{H} \parallel \hat{c}$ and \hat{a} , respectively.

results show that the holelike carrier number n_h almost does not change with T even across the MIC at T_{\min} . On the other hand, the MIC seemingly corresponds to a broad peak in the holelike mobility μ_h [Fig. 7(c)], at which its behavior changes from increasing to decreasing with cooling down. For the data at $T < T^*$, since a non-linear Hall effect is often interpreted as a signature of a competition between electronlike and holelike carriers²⁶, we tried a semiclassical two-carrier-type fitting [see Sec.V]. The results of the two-carrier-types fits suggest an abrupt emergence of electronlike carriers with much lower number (n_e) and higher mobility (μ_e), and an increase of n_h as T decreases. Such changes in carrier numbers are usually accompanied by a magnetic phase transition or structural distortion, but none of which can be detected (see sections IID and IIE). Furthermore, attempts to fit the data using the two-carrier-type model in the temperature window between 20 K and 40 K yield scattered values of number and mobility for the electronlike carriers. This is due to the small curvature of the $\rho_{yx}(H_c)$ in this temperature window and the highly nonlinear formula for the two-carrier-type Hall effect shown in Eq. (5). The two-band analysis, and the emergence of the electronlike carriers as its result, may not be a reliable estimation for the current

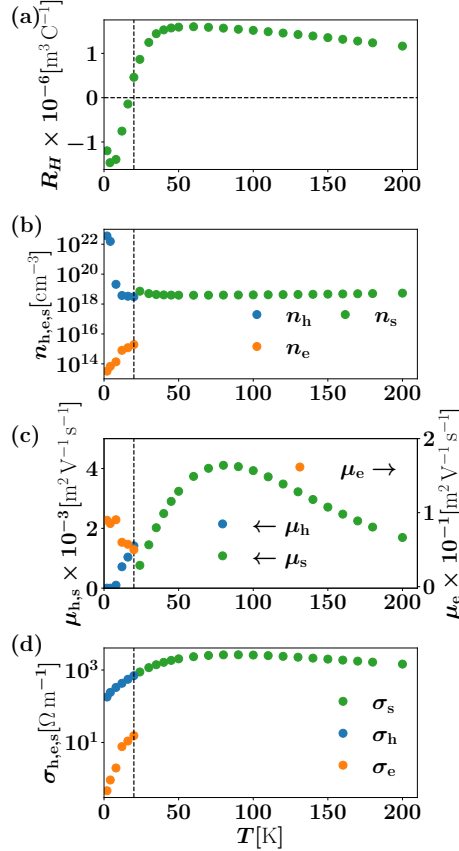


Fig. 7. (Color online) Temperature dependence of (a) Hall coefficient calculated from the slope near the zero-field region of Hall resistance. (b) Hall carrier density, (c) mobility and (d) effective conductivity calculated from the fitting of Hall resistivity utilizing a single carrier model at $T > 20$ K and a two-carrier mode at $T \leq 20$ K, respectively. We note that the reliability of the data points at $T \leq 20$ K can be questionable due to the validity of the two-carrier-type model in the context of BaMn₂Bi₂ (see text).

case. The nonlinear Hall effect may come from another reason outside the framework of the semiclassical theory.

As shown in Fig. 6(b), the current-out-of-plane Hall effect is similar to that obtained from the current-in-plane settings for $T > T^*$, the positive slopes of the linear ρ_{yz} curves consistently indicate the dominating contribution of holelike carriers. However, at $T < T^*$, the current-out-of-plane setting yields more complex Hall resistivity curve. Here $\mathbf{H} \parallel a$ and $\mathbf{j} \parallel c$, and the complex 2-component LNMR simultaneously manifest in this configuration. Therefore $\rho_{xz}(H_a)$ can be sensitively influenced by the strength of the H_a . On the other

hand, the $\rho_{xz}(H_a)$ curves in this regime approach to a linear line with positive slope under high H_a 's. In the $T > T^*$ regime, the Hall effect is positive and linear, indicating that holelike carriers govern the transport properties.

D. Thermodynamics

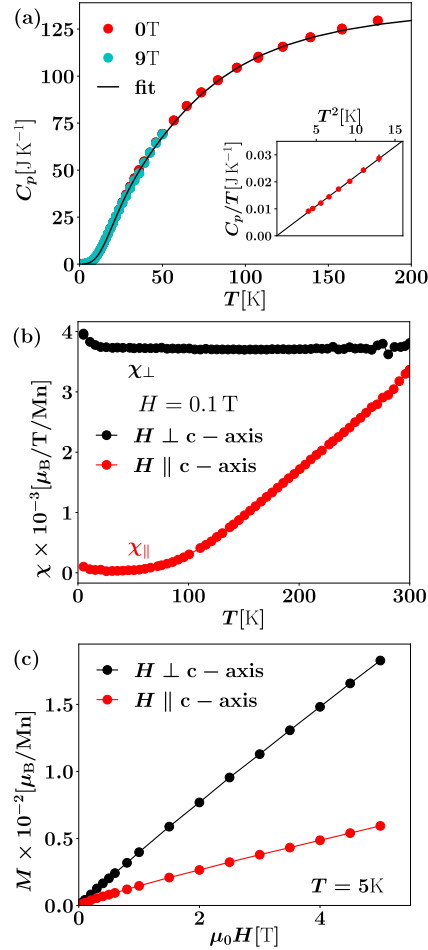


Fig. 8. (Color online) (a) Temperature dependence of specific heat (C_p) of BMBi. Analyses were made by employing the Einstein and the Debye model. Inset is the C_p/T v.s. T^2 plot (red circle) and its theoretical fitting (black line) using the equation of $\gamma T + \beta T^3$. (b) Anisotropic temperature dependence of magnetic susceptibility (χ) evaluated at $\mu_0 H = 0.1$ T applied along the \hat{a} -axis and the \hat{c} -axis. (c) Magnetic field dependence of magnetic moment (M) per Mn ion.

In order to investigate other additional effects of the in-plane magnetic fields to the electronic properties, we measured the isobaric specific heat C_p under $\mu_0 H_a = 0$ T and

9 T [Fig. 8 (a)]. We observed no signature of phase transition and the $C_p(T)$ curve is well-described by a summation of the Debye and the Einstein terms, $C_p \approx C_v^D + C_v^E$ (see sec. V). A linear fit to C_p/T plotted versus T^2 at $T \leq 5$ K yields an almost zero Sommerfeld coefficient $\gamma \approx 0 \text{ mJ K}^{-2}$ [Fig. 8(a), inset]. This indicates a very small number of free carriers in this system, and it is reasonable considering the small number of charge carriers found by transport properties.

E. Magnetism

In Fig.8(b) we show the T -dependence of the magnetic susceptibilities $\chi_{\perp}(T)$ and $\chi_{\parallel}(T)$ measured under \mathbf{H} perpendicular and parallel to the easy c -axis, respectively. The difference between χ_{\perp} and χ_{\parallel} shows a typical anisotropy of a colinear AFM between the ab -plane and the \hat{c} -axis (easy axis). The Néel temperature T_N estimated from the extrapolation is comparable to that obtained from previous studies^{22,24}. We note that a Curie tail was observed in both $\chi_{\perp}(T)$ and $\chi_{\parallel}(T)$. We found that the magnitude of this component is different among samples, and the older samples show the larger Curie tails. This reminds us about the mild sensitivity of BaMn_2Bi_2 with respect to the moisture²². At the moment, we thus attribute the Curie tail to the contribution of the degradation of the samples. On the other hand, the H -dependence of magnetization (M) at $T = 5$ K is linear up to $H = 5$ T [Fig.8(c)]. No indication of phase transition is also given from the viewpoint of magnetization measurements as well as specific heat measurements.

III. DISCUSSION

The most important feature in the transport properties of BaMn_2Bi_2 is MIC seen in the T -dependence of the resistivities (Figs. 2 and Figs. 4) at $T_{\min} \approx 83$ K being far from the Néel temperature T_N . Our thermodynamic and magnetic measurements did not reveal any signatures of a structural or magnetic transition even at high H_{ab} . On the other hand, a recent theoretical calculation shows that the MICs observed in BaMn_2Pn_2 antiferromagnets are the consequences of a Mott localization of holelike states around the E_F ¹⁹. At low temperatures, the strong Mott localization results in the insulating behaviors observed in the transport resistivities. Its strength is weakened by increasing temperature, so that a

cross-over to metallic behaviors is expected. For the case of BaMn₂Bi₂ shown here, the dependencies on temperature of the carrier number and the mobility (Fig. 7) suggest that the MIC is caused by a vanishing mobility μ_h of holelike carriers that occupy the states at the top of the d - p valence band. This is qualitatively in a good agreement with the picture of Mott localized holelike carriers shown in Ref. [19]. Interestingly, this Mott-like MIC can be reversed via the LNMR under \mathbf{H}_{ab} , and a metallic behavior appears in the resistivity curves in the whole T -range. If the carrier number is unaffected by \mathbf{H}_{ab} , then the LNMR corresponds to an enhanced μ_h at all temperatures below T_{\min} . The metallic state under high \mathbf{H}_{ab} is accordingly equivalent to a metallic T -dependence of μ_h , i.e. μ_h increases as T decreases. We note that in order to confirm this scenario, a direct measurement of both carrier number and mobility as a function of \mathbf{H}_{ab} is necessary.

A key feature in the transport properties of BaMn₂Bi₂ is the anisotropy of the resistivity tensor for various directions of \mathbf{j} and \mathbf{H} . In both current-in-plane and current-out-of-plane settings, the LNMR is maximized when \mathbf{H} is perpendicular to the AFM Néel vector, the later is pinned along the \hat{c} -axis by a large exchange interaction $H_{\text{exchange}} \approx 250$ T. Under $H_{ab} \approx 16$ T, BaMn₂Bi₂ can be regarded as a metal in both ρ_a and ρ_c thanks to the saturation of the LNMR; nevertheless the AFM sublattices magnetization are merely canted a infinitesimal angle in these magnetic fields. The extreme sensitivity of the MIC to a minute canting of the G-AFM is intriguing, and its mechanism may involve the multi-orbital nature gaining its importance at the vicinity of a Mott transition of BaMn₂Bi₂¹⁹. Another appealing mechanism may come from the breaking of AFM protected PT symmetry via \mathbf{H}_{ab} . In this scenario, even a small canting of the AFM moments breaks PT symmetry and the metallic behavior under \mathbf{H}_{ab} represents a state of a broken symmetry.

Finally, we would like to come back to the T -dependencies of the carrier numbers and the mobilities obtained from our analyses of the transverse Hall effect under $H_{ab} = 0$. The number of the dominant holelike carriers estimated from the Hall coefficients at $T > T^*$, i.e. in the linear regime of the ρ_{yx} curves, is approximately $4 \times 10^{19} \text{ cm}^{-3}$, or 1.2×10^{-3} holes per unit cell. Given the DOS of the calculated band structure, the estimated density of holes is equivalent to an E_F at about 10 meV lower than the top of the valence band. Such placement of E_F is consistent with the fact that the holelike carrier number stays almost constant across T_{\min} and suggests that BaMn₂Bi₂ can be regarded as a highly degenerated semiconductor. The reduction of μ_h with decreasing T attributed as the cause of the MIC

is clearly seen in this linear regime of ρ_{yx} . At $T < T^*$, if we ignore the non-linear ρ_{yx} curves by assuming that the number of holelike carrier is constant, we will obtain a μ_h being decay to zero with decreasing T , i.e. being similar to Fig. 7(c). On the other hand, the non-linear ρ_{yx} curves with a negative slope in this regime is rather curious.

A nonlinear Hall effect is often interpreted as a signature of a two-carrier-type system. The results of our analysis using a conventional two-carrier-type model suggests an abrupt occurrence of an electron-like carrier type, but the conclusion has not presently been supported by any experimental observations such as magnetic and thermodynamic measurements. Alternatively, there is another explanation for a negative Hall effect, which may be more plausible in the case of BaMn_2Bi_2 . Fig. 2(a) shows that, at $T \leq T^*$, the temperature dependence of the resistivity of BaMn_2Bi_2 enters a VRH regime, i.e. $\rho \propto \exp [(T_0/T)^{1/4}]$. Being caused by the hopping motions in a close path, even holelike carriers can exhibit a negative Hall effect in this regime^{27,28}. As the temperature increases, the VRH ceases to be valid allowing the Hall effect to gradually change to back to positive. In this scenario, the electronlike carrier does not exist, and what we observed in the Hall effect is holelike carrier in the VRH regime. The positive component of the MR observe in BaMn_2Bi_2 may also arise from the VRH conduction of holelike carriers under magnetic fields²⁹.

IV. SUMMARY

We reported transport, thermodynamic, and magnetic properties of AFM BaMn_2Bi_2 single crystals. BaMn_2Bi_2 exhibits a MIC being far away from the Néel temperature which is not related to any structural and/or magnetic transitions, as shown by the measurements of specific heat and magnetic susceptibility. In the insulating regime, the conductivity of BaMn_2Bi_2 exhibits a very large enhancement when a magnetic field is applied perpendicular to the Néel vector of the AFM order and a metallic state seems to be fully recovered, which is the origin of the observed negative LNMR. Our analyses of the electrical transport properties showed that the MIC and the LNMR are likely due to the change in carrier mobility varying with T and H_{ab} .

V. METHOD

A. DFT calculation

Wien2k package was used to calculate the electronic structure of BaMn_2Bi_2 . The lattice parameters $a = b$, c and z_{Bi} are referred from previous study²². The generalized gradient approximation (GGA) by Perdew, Burke, and Ernzerhof (PBE)³⁰ exchange-correlation potential was chosen. The radii of the muffin-tin sphere RMT were 2.5 bohrs for all atoms. A $15 \times 15 \times 15$ k-point mesh was utilized in the self-consistent calculations. The truncation of the modulus of the reciprocal lattice vector K_{max} , which was used for the expansion of the wave functions in the interstitial regions, was set to $RMT \times K_{max} = 7$. All calculation was done with assumption of G-type AFM ordering. DFT calculation including spin-orbit coupling via the option of Wien2k package was also conducted. The other DFT calculation package, Quantum Espresso, was also used for comparison and Any significant difference were not found.

B. Synthesis

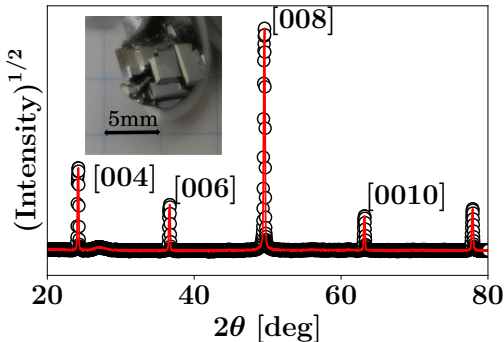


Fig. 9. The crystalline X-ray diffraction spectrum along \hat{c} -axis. Inset is a photo of single crystals grown in alumina crucible.

Single crystals of BaMn_2Bi_2 were grown out from the metallic Bi-flux following the method described in Ref. 22. In brief, a mixture of Ba, Mn, and Bi with the molar ratio $\text{Ba} : \text{Mn} : \text{Bi} = 1 : 2 : 5$ was loaded into a Al_2O_3 crucible and then was sealed in a fused-silica tube under helium atmosphere. The ampule was put into an electric furnace and the temperature was increased to 1000°C in 10 hours, then kept for 10 hours to ensure complete

reactions between the chemicals. The temperature was then slowly cooled down at the rate of 2°C h^{-1} to 500°C , at which centrifugal decanting was performed to remove the excess Bi flux. Large single crystals of centimeter-size and mirror ab surfaces were obtained from the described growth process as shown in inset of Fig. 9. It is noted that BaMn_2Bi_2 single crystals are fairly sensitive to oxygen and moisture in air²² and therefore were kept either in vacuum or in an Argon-filled glovebox.

C. Single Crystal Characterization

In order to characterize our single crystals, X-ray diffraction (XRD) measurement done with the help of a RIGAKU SmartLab X-ray Diffractometer. The chemical composition of the single crystals were confirmed by energy dispersive X-ray spectroscopy (EDX) measurement employing a JEOL JSN-7800 scanning electron microscope quipped with an Oxford X-MAX50 analyzer. Fig.9 shows the result of Crystal XRD and the picture of single crystal. $[00l]$ (l is even due to the body-centered structure) peaks were obtained. The lattice constant is $c = 14.45$ which is comparable to previous work by Saporov *et.al*, 14.687. The broad peak around 26° is due to the oxidation on the surface. It can be seen in EDX.

The result of EDX indicates the inclusion of a little amount of oxygen due to the oxidation on the surface. The ratio after the oxidation subtraction is close to the ideal one i.e. $\text{Ba}:\text{Mn}:\text{Bi} = 1:2:2$. The fluctuation of ratio is below 1%.

D. Measurements and analysis

In order to prepare the samples for the measurements, BaMn_2Bi_2 single crystals were cleaved to remove excessive flux and to expose fresh ab -surfaces. Due to the sensitivity to air of the compound, care were taken so that the samples were exposed less than 2 hours in the air. The crystals selected for transport measurements were cut into rectangular shapes whose edges were aligned along the a and b . For the measurements of longitudinal resistivity (ρ) and Hall resistivity (ρ_{yx}), six silver-paste electrodes were made on the sample so that the electric current \mathbf{j}_E could be applied along the \hat{a} -axis. The T - and \mathbf{H} -dependencies of ρ and ρ_{yx} under were first measured under $\mu_0 H \leq 9\text{ T}$ using a Quantum Design Physical Property Measurement System (PPMS). Here H denotes the magnitude of the magnetic field \mathbf{H} .

We also measured the transport properties under $\mu_0 H \leq 18$ T employing a JASTEC 18 T superconducting magnet at High Field Laboratory (HFL), Institute for Material Research, Tohoku University. We also utilized a 55 T pulse magnet at the Center for Advanced High Magnetic Field Science (AHMF), Osaka University to probe the transport properties under extreme H . In these experiments, the measurements of angle-resolved MR with \mathbf{H} rotating in the ab and the ac -plane of the crystals were also conducted with the help of sample rotators.

The magnetoresistance (MR) is defined as:

$$\text{MR}(H, \theta, \phi) = \frac{\rho(H, \theta, \phi) - \rho_0}{\rho_0}. \quad (1)$$

Here ρ_0 is the resistivity under $H = 0$, and θ and ϕ are defined in Fig. 3(a) and (c), respectively.

We carried out the analyses of the in-plane Hall effect ρ_{yx} as follows. At first, we evaluated the carrier numbers using a one-carrier-type model in the $T > T^*$ regime;

$$\rho_{yx} = R_{\text{H}} \mu_0 H_c. \quad (2)$$

Here R_{H} is the Hall coefficient and is related to the carrier number n_{H} and mobility μ_{H} as;

$$n_{\text{H}} = \frac{1}{e R_{\text{H}}}. \quad (3)$$

$$\mu_{\text{H}} = \frac{1}{e n_{\text{H}} \rho_0}. \quad (4)$$

The analyses were carried out by fitting Eq. (2) to the $\rho_{yx}(H_c)$ experimental data [Fig. 6]. At $T \lesssim 30$ K, where $\rho_{yx}(H_c)$ is strongly non-linear, we employed a linear fit in a small H_c window around 0, $\mu_0 |H_c| < 1$ T.

The a two-carrier-type model that was used to analyzed the non-linear $\rho_{yx}(H_c)$ at $T \lesssim 40$ K is;

$$\rho_{yx} = \frac{1}{e} \frac{\mu_h^2 \mu_e^2 (n_h - n_e) (\mu_0 H_c)^3 + (\mu_h^2 n_h - \mu_e^2 n_e) (\mu_0 H_c)}{\mu_h^2 \mu_e^2 (n_h - n_e)^2 (\mu_0 H_c)^2 + (\mu_h n_h + \mu_e n_e)^2}. \quad (5)$$

Here, n_i and μ_i denote the carrier density and the mobility; the subscripts e and h denote the electron- and the hole- carriers, respectively.

In our analysis, at first we fit a nonlinear $\rho_{yx}(H_c)$ curve by the following equation;

$$\rho_{yx}(H_c) = \frac{a(\mu_0 H_c)^3 + b H_c}{c(\mu_0 H_c)^2 + 1}. \quad (6)$$

We note that there are only three fitting parameters in Eq. (6). Since the last term in the denominator of the RHS in Eq. (6) is fixed to 1, the degrees of freedom in the determination of the other three parameters in Eq. (6) by fitting are greatly reduced. Now, using Eq. (5), a , b , and c are related to n_i 's and μ_i 's as follows.

$$a = \frac{e\mu_h^2\mu_e^2(n_h - n_e)}{\sigma_0^2}, \quad (7a)$$

$$b = \frac{e(\mu_h^2n_h - \mu_e^2n_e)}{\sigma_0^2}, \quad (7b)$$

$$c = \frac{e^2\mu_h^2\mu_e^2(n_h - n_e)^2}{\sigma_0^2}, \quad (7c)$$

$$\sigma_0 = e(\mu_hn_h + \mu_en_e). \quad (7d)$$

As explained above, σ_0 in Eq. (7d) can be measured independently. By solving the system of equations (7), we can obtain n_i 's and μ_i 's.

This procedure, fixing one of the fitting parameters, is essential in practice. Otherwise, if four parameters had been used in the fitting function in the RHS of Eq. (6), i.e. the last term in the denominator had been an additional free parameter d , they would have not been determined uniquely. This is because when the all four parameters are multiplied by a factor, they will produce the same fitting curve, but the obtained values of n_i 's and μ_i 's can be spuriously wrong due to relations shown in Eqs (7).

The isobaric specific heat C_p of BaMn₂Bi₂ was measured in the T range from 2 K to 200 K and under various B -strengths using the commercial heat capacity option of PPMS. A single crystalline sample was fixed at the center of the PPMS calorimeter puck by Apiezon N grease so that the direction of \mathbf{H} was parallel to the \hat{a} axis. Puck calibration as well as addenda measurements were done at each B -strength to minimize the possible errors. The temperature dependence of the specific heat was fitted using the following model;

$$C_p \approx C_v^D + C_v^E; \quad (8)$$

with $C_v^D = 9Nk_B \left(\frac{k_B T}{\hbar\omega_D}\right)^3 \int_0^{x_D} \frac{x^4 e^x}{(e^x - 1)^2} dx$ and $C_v^E = 3Nk_B \left(\frac{k_B T}{2\hbar\omega_E}\right)^2 \left/ \sinh^2\left(\frac{k_B T}{2\hbar\omega_E}\right)\right.$, respectively. Here N is the number of atoms per unit cell and k_B the Boltzmann constant. The Debye ω_D and the Einstein frequency ω_E were used as fitting parameters and x_D is the dimensionless Debye number defined as $x_D \equiv \frac{\hbar\omega_D}{k_B T}$. The calculation using the model with least-squared algorithm (the Python package Scipy³¹) well fitted the experimental data as shown in Fig. 8(c).

The magnetizations of BaMn₂Bi₂ single crystals were measured using a Quantum Design Magnetic Property Measurement System (MPMS) along the *ab*-plane and the \hat{c} -axis. In this measurements, samples fixed by GE-vanish onto a holder made from a thin rod of fused silica.

In the framework of the mean field theory, the Hamiltonian of one spin \mathbf{S}_0 under the external magnetic field H_{ext} perpendicular to the \hat{c} -axis can be described by the exchange interaction and Zeeman energy i.e.

$$\begin{aligned} \mathcal{H}_{spin} = & (z_1 J_1 \mathbf{S}_1 + z_2 J_2 \mathbf{S}_2 + z_c J_c \mathbf{S}_c) \cdot \mathbf{S}_0 \\ & - D S_{0,\parallel}^2 + g \mu_B \mathbf{S}_0 \cdot \mathbf{H}_{ext} \end{aligned} \quad (9)$$

Here, \mathbf{S}_1 , \mathbf{S}_2 and \mathbf{S}_c are nearest, second nearest and inter-plane nearest spins. And J s are each exchange interaction. the other square and linear terms of \mathbf{S}_0 are anisotropic term and Zeeman term. The second term including $\mathbf{S}_2 \cdot \mathbf{S}_0$ make no energy change depending on external field because the angle between these two spins might be zero for any strength of magnetic field. Assuming θ , the angle of spin from \hat{c} -axis, the spin can be decomposed to two parts. One is parallel to \hat{c} -axis and described by $S \cos \theta$, where S is the magnitude of spin moment. The other is $S \sin \theta$ that is parallel to H_{ext} . Due to the antiferromagnetic ordering, the former changes the sign for each nearest neighbor. The Hamiltonian can be rewritten based on these assumptions as

$$\begin{aligned} \mathcal{H}_{spin} = & (z_1 J_1 + z_c J_c) S^2 (\sin^2 \theta - \cos^2 \theta) - \\ & D S^2 \cos^2 \theta - g \mu_B S \sin \theta H_{ex} \end{aligned} \quad (10)$$

$$\begin{aligned} \frac{\partial \mathcal{H}_{spin}}{\partial \theta} = & [4(z_1 J_1 + z_c J_c) + 2D] S^2 \sin \theta \cos \theta - \\ & g \mu_B S H_{ex} \cos \theta \end{aligned} \quad (11)$$

There is the angle θ_0 that minimize the energy as $\left. \frac{\partial \mathcal{H}_{spin}}{\partial \theta} \right|_{\theta_0} = 0$. As a result,

$$\theta_0 = \frac{g \mu_B H_{ex}}{4(z_1 S J_1 + z_c S J_c) + 2SD} \quad (12)$$

$$m_{\perp} = g \mu_B S_{\perp} \approx \frac{g^2 \mu_B^2 H_{ex}}{4(z_1 S J_1 + z_c S J_c) + 2SD} \quad (13)$$

$$\chi_{\perp} = \frac{2m_{\perp}}{H_{ex}} = \frac{2g^2 \mu_B}{4(z_1 S J_1 + z_c S J_c) + 2SD} [\mu_B / \text{T} / \text{unit_cell}] \quad (14)$$

Here, m_{\perp} is a magnetization for one Mn-site and it is doubled when χ_{\perp} calculation because one unit cell contain two Mn's. The experimental values $SJ_1 = 21.7 \text{ meV}$, $SJ_c =$

1.26 meV, $SD = 0.046 \text{ meV}^{24}$ result $\chi_{\perp} = 12.96 \times 10^{-3} [\mu_B/\text{T} \cdot \text{unit_cell}]$ that is twice as the experimental result shown in Fig.8(a). The effective field from exchange interaction also calculated from Eq. (9) that approximately results 250 T as mentioned in Section II E.

ACKNOWLEDGEMENTS

We thank K. Ogushi, T. Aoyama, K. Igarashi, H. Watanabe, Y. Yanase, and T. Arima for fruitful discussions. This work was supported by a Grant-in-Aid for Scientific Research on Innovative Areas “J-Physics” (Grant No.18H04304), and by JSPS KAKENHI (Grants No. 18K13489, No. 18H03883, No. 17H045326, and No. 18H03858). T.O. thanks the financial supports from the International Joint Graduate Program in Materials Science (GP-MS) of Tohoku University. Experiments under high magnetic fields was done at High Field Laboratory for Superconducting Materials (HFLSM) in Tohoku University. Pulsed field measurements were carried out at the Center for Advanced High Magnetic Field Science in Osaka University under the Visiting Researcher’s Program of the Institute for Solid State Physics, the University of Tokyo. This research was partly made under the financial support by the bilateral country research program of JSPS between AIMR, Tohoku University and Jozef Stefane Institute, Slovenia. This work was also supported by World Premier International Research Center Initiative (WPI), MEXT, Japan. DA acknowledges the financial support of the Slovenian Research Agency through BI-JP/17-19-004 and J1-9145 grants.

* huynh.kim.khuong.b4@tohoku.ac.jp

† katsumi.tanigaki.c3@tohoku.ac.jp

¹ R. Hoffmann and C. Zheng, *J. Phys. Chem.* **89**, 4175 (1985).

² M. Rotter, M. Tegel, and D. Johrendt, *Physical Review Letters* **101**, 107006 (2008).

³ P. L. Alireza, Y. T. C. Ko, J. Gillett, C. M. Petrone, J. M. Cole, G. G. Lonzarich, and S. E. Sebastian, *Journal of Physics: Condensed Matter* **21**, 012208 (2009).

⁴ D. J. Singh, A. S. Sefat, M. A. McGuire, B. C. Sales, D. Mandrus, L. H. VanBebber, and V. Keppens, *Physical Review B* **79**, 094429 (2009).

- ⁵ K. A. Filsinger, W. Schnelle, P. Adler, G. H. Fecher, M. Reehuis, A. Hoser, J.-U. Hoffmann, P. Werner, M. Greenblatt, and C. Felser, *Physical Review B* **95**, 184414 (2017).
- ⁶ A. S. Sefat, D. J. Singh, R. Jin, M. A. McGuire, B. C. Sales, and D. Mandrus, *Physical Review B* **79**, 024512 (2009).
- ⁷ R. S. Dhaka, Y. Lee, V. K. Anand, D. C. Johnston, B. N. Harmon, and A. Kaminski, *Physical Review B* **87**, 214516 (2013).
- ⁸ A. van Roekeghem, T. Ayrat, J. M. Tomczak, M. Casula, N. Xu, H. Ding, M. Ferrero, O. Parcollet, H. Jiang, and S. Biermann, *Physical Review Letters* **113**, 266403 (2014).
- ⁹ K. Ahilan, T. Imai, A. S. Sefat, and F. L. Ning, *Physical Review B* **90**, 014520 (2014).
- ¹⁰ D. J. Singh, *Physical Review B* **79**, 153102 (2009).
- ¹¹ S. F. Wu, P. Richard, A. van Roekeghem, S. M. Nie, H. Miao, N. Xu, T. Qian, B. Saparov, Z. Fang, S. Biermann, A. S. Sefat, and H. Ding, *Physical Review B* **91**, 235109 (2015).
- ¹² A. Subedi and D. J. Singh, *Physical Review B* **78**, 132511 (2008).
- ¹³ N. Kurita, F. Ronning, Y. Tokiwa, E. D. Bauer, A. Subedi, D. J. Singh, J. D. Thompson, and R. Movshovich, *Physical Review Letters* **102**, 147004 (2009).
- ¹⁴ K. Zhao, Z. Deng, X. C. Wang, W. Han, J. L. Zhu, X. Li, Q. Q. Liu, R. C. Yu, T. Goko, B. Frandsen, L. Liu, F. Ning, Y. J. Uemura, H. Dabkowska, G. M. Luke, H. Luetkens, E. Morenzoni, S. R. Dunsiger, A. Senyshyn, P. Böni, and C. Q. Jin, *Nature Communications* **4**, 1442 (2013).
- ¹⁵ H. Man, S. Guo, Y. Sui, Y. Guo, B. Chen, H. Wang, C. Ding, and F. L. Ning, *Scientific Reports* **5**, 15507 (2015).
- ¹⁶ H. Suzuki, K. Zhao, G. Shibata, Y. Takahashi, S. Sakamoto, K. Yoshimatsu, B. J. Chen, H. Kumigashira, F.-H. Chang, H.-J. Lin, D. J. Huang, C. T. Chen, B. Gu, S. Maekawa, Y. J. Uemura, C. Q. Jin, and A. Fujimori, *Physical Review B* **91**, 140401 (2015).
- ¹⁷ B. Gu and S. Maekawa, *Physical Review B* **94**, 155202 (2016).
- ¹⁸ H. Watanabe and Y. Yanase, *Physical Review B* **96**, 064432 (2017).
- ¹⁹ L. Craco and S. S. Carara, *Physical Review B* **97**, 205114 (2018).
- ²⁰ K.-K. Huynh, T. Ogasawara, K. Kitahara, Y. Tanabe, S. Y. Matsushita, T. Tahara, T. Kida, M. Hagiwara, D. Arčon, and K. Tanigaki, *Physical Review B* **99**, 195111 (2019).
- ²¹ P. Blaha, K. Schwarz, G. K. H. Madsen, D. Kvasnicka, J. Luitz, R. Laskowski, F. Tran, and L. D. Marks, *WIEN2k: An Augmented Plane Wave plus Local Orbitals Program for Calculating Crystal Properties* (Vienna University of Technology, Austria, 2018).

- ²² B. Saparov and A. S. Sefat, *Journal of Solid State Chemistry* **204**, 32 (2013).
- ²³ W.-L. Zhang, P. Richard, A. van Roekeghem, S.-M. Nie, N. Xu, P. Zhang, H. Miao, S.-F. Wu, J.-X. Yin, B. B. Fu, L.-Y. Kong, T. Qian, Z.-J. Wang, Z. Fang, A. S. Sefat, S. Biermann, and H. Ding, *Phys. Rev. B* **94**, 155155 (2016).
- ²⁴ S. Calder, B. Saparov, H. B. Cao, J. L. Niedziela, M. D. Lumsden, A. S. Sefat, and A. D. Christianson, *Phys. Rev. B* **89**, 064417 (2014).
- ²⁵ Z. Tian, Y. Kohama, T. Tomita, H. Ishizuka, T. H. Hsieh, J. J. Ishikawa, K. Kindo, L. Balents, and S. Nakatsuji, *Nature Physics* **12**, 134 (2015).
- ²⁶ K. K. Huynh, Y. Tanabe, T. Urata, S. Heguri, K. Tanigaki, T. Kida, and M. Hagiwara, *New J. Phys.* **16**, 093062 (2014).
- ²⁷ L. Friedman, *Journal of Non-Crystalline Solids* **6**, 329 (1971).
- ²⁸ N. F. Mott and E. A. Davis, *Electronic processes in non-crystalline materials*, 2nd ed., The international series of monographs on physics (Oxford Univ. Press, Oxford, 2012).
- ²⁹ A. Kurobe and H. Kamimura, *Journal of the Physical Society of Japan* **51**, 1904 (1982).
- ³⁰ J. P. Perdew, K. Burke, and M. Ernzerhof, *Physical Review Letters* **77**, 3865 (1996).
- ³¹ E. Jones, T. Oliphant, P. Peterson, *et al.*, “SciPy: Open source scientific tools for Python,” (2001–).